The Meteoritical Society

Meteoritics & Planetary Science 43, Nr 1/2, 121–134 (2008)
Abstract available online at http://meteoritics.org

Origin and formation of iron silicide phases in the aerogel of the Stardust mission

Frans J. M. RIETMEIJER[1*], Tomoki NAKAMURA[2], Akira TSUCHIYAMA[3], Kentaro UESUGI[4], Tsukasa NAKANO[5], and Hugues LEROUX[6]

[1]Department of Earth and Planetary Sciences, MSC03-2040, University of New Mexico, Albuquerque, New Mexico 87131–0001, USA
[2]Department of Earth and Planetary Science, Faculty of Science, Kyushu University, Hakozaki, Fukuoka 812-8581, Japan
[3]Department of Earth and Space Science, Graduate School of Science, Osaka University, Toyonaka 560-0043, Japan
[4]Japan Synchrotron Radiation Research Institute, SPring-8, Sayo, Hyogo 679-5198, Japan
[5]Geological Survey of Japan, National Institute of Advanced Industrial Science and Technology, Tsukuba 305-8567, Japan
[6]Laboratoire de Structure et Propriétés de l'Etat Solide, UMR 8008, Université des Sciences et Technologies de Lille, F-59655 Villeneuve d'Ascq, France
[*]Corresponding author. E-mail: fransjmr@unm.edu

(Submitted 17 December 2006; revision accepted 19 April 2007)

Abstract–Suessite along with hapkeite and more Fe-rich iron-silicides up to Fe_7Si_2 formed near the entrance of aerogel track #44. These phases are ~100 nm, quenched-melt spheres, but the post-impact cooling regime was such that melt vitrification produced a polycrystalline mixture of Fe silicides and kamacite. The compositional similarities of the impact-produced Fe-Si phases and the Fe-Ni-S phases scattered throughout the aerogel capture medium strongly supports the idea that Fe silicides resulted from a reaction between molten Fe-Ni-S phases and aerogel at very high heating and cooling rates. Temperatures of around 1500 °C are inferred from the observed compositions had the silicide spheres formed at thermodynamic equilibrium, which seems unlikely. When the conditions were kinetically controlled, they could have been similar to those leading to the formation of solids with predictable deep metastable eutectic compositions in laboratory condensation experiments.

INTRODUCTION

The NASA Stardust mission was launched on February 7, 1999, and had an encounter with Jupiter-family comet 81P/Wild 2 on January 2, 2004. It became an unqualified success when on January 15, 2006, it ended with the delivery to Earth of the first collected dust sample of a known active comet (Zolensky et al. 2006). Comet nuclei are considered repositories of the dust that accreted in the early Solar System beyond the orbit of Uranus and stretching all the way into the vast reaches of the Edgwood-Kuiper Belt. It is anticipated that interstellar materials will be among the accreted dust in comet nuclei. Thus, the stakes are high to fully appreciate the original comet nucleus debris that was captured in the silica aerogel cells of the Stardust comet dust collector. It was known from laboratory experiments that hypervelocity impact capture of Wild 2 dust at 6.1 km/s would cause modification of original dust properties to variable extents (Barrett et al. 1992; Okudaira et al. 2004, 2005; Burchell et al. 2006). Indeed, the Preliminary Examination (PE) team found indications of modification of Wild 2 dust, such as shattering of silicate and sulfide minerals and Ni-free and low-Ni Fe sulfide melting (Zolensky et al. 2006). More subtle features might exist, such as spherical melt droplets that superficially resemble the ferromagnesiosilica units of glass with embedded metal and sulfides (GEMS) (Bradley 1994) in the matrix of many aggregate interplanetary dust particles (Rietmeijer 1998, 2002).

At this time, only rough estimates of peak heating temperatures experienced by comet dust during impact capture range from ~1100 °C and higher (Zolensky et al. 2006). It is not yet clear how much and at what rates heat was dissipated on local scales in under-dense (0.02 g/cm^3) aerogel, which is in fact a perfect thermal insulator (Okudaira et al. 2005) and which could cause as-yet unquantified thermal annealing. The aerogel of track walls, and penetrating some distance into the aerogel cell, often display a shotgun pattern of Fe-Ni-S nanophases. The mineralogical analyses of the captured dust distributed along the entire track length and offshoots from the main track could be used to constrain peak-heating thermal regimes.

We report on Fe-Si phases found scattered within the silica aerogel capture medium among numerous inclusions of Fe,Ni metal and low-S Fe-Ni-S phases. Silicides are stable at very low oxygen partial pressures in extraterrestrial environments (Keil et al. 1982; Anand et al. 2004) and in extremely reducing,

ultrahigh-temperature, transient terrestrial environments, such as fulgurites (Essene and Fisher 1986). Equilibrium condensation models showed Fe-Si solid solution formation between 1053–1185 °C, C/O = 1.2–0.55, and 10^{-3} atm in the solar nebula, but no Fe-Si solids would form in supernova ejecta (Lattimer and Grossman 1978). Silicides were not yet reported in a rich interstellar grain population preserved in meteorites and interplanetary dust particles (IDPs). Lacking stable isotope signatures for the Fe-Si phases reported here, an interstellar origin is not explored to explain their presence in Stardust mission silica aerogel capture cells.

ANALYTICAL TECHNIQUES

The allocations were prepared from grains taken off of a small piece of aerogel at the front of cometary track #44 of cell C2004 from which three grains, C2004,1,44,1,0, C2004,1,44,2,0, and C2004,1,44,3,0 were studied. This track is the largest impact feature on the entire cometary collector and is in fact a secondary impact feature. The cometary particle first struck the aluminum frame of the collector, and then material from both the impacted particle and the Au foil-coated Al tray together made the huge track #44, which was classified as a hedgehog-type track. It penetrated to a depth of ~0.8 cm into the aerogel.

For the purposes of this paper, we use "grain" to refer to a physically coherent, micron-sized entity without any presumption of its petrographic fabric. All sample preparation prior to allocation was performed at the NASA Johnson Space Center Stardust Curatorial Facility. This procedure minimizes the risk of extraneous material compromising the samples. These three grains were first analyzed by synchrotron X-ray diffraction (SXRD). Each grain was mounted on a thin glass fiber 3 μm thick using a small amount acetone-soluble bond and placed in the Gandolfi camera for exposure to synchrotron X-rays with a wavelength of 2.161 ± 0.001 Å for 3 h to produce a powder X-ray diffraction pattern. The analyses were performed at beam line 3A of the Photon Factory Institute of Material Science, High-Energy Accelerator Research Organization (for details of these procedures, see Nakamura et al. 2008). Following SXRD analyses, grains C2004,1,44,1,0 and C2004,1,44,2,0 were imaged and analyzed by SEM/EDS at NASA/JSC (Zolensky et al. 2006). Grain C2004,1,44,3,0 was imaged and analyzed by microtomography at beam line BL47XU of Japan Synchrotron Radiation Research Institute (SPring-8). The imaging experiments were made using imaging tomography (Uesugi et al. 2006) at 8 keV with 3600 projections for each slice. Three-dimensional structures were obtained from 490 slice images with a voxel (pixel in 3-D) size of 42.5 × 42.5 × 42.5 nm. The solid portion (whole grain) and the highly absorbed portion that might correspond to Fe-Si or Fe-Ni-S phases were obtained by thresholding the CT-image contrast (for details of the procedures, see Nakamura et al. 2008).

Grain C2004,1,44,1,0 was treated and washed severely in acetone and glycolphthalate for preparation for synchrotron analyses. Subsequently, acetone was used to remove it for embedding in epoxy to prepare 70 nm thick serial ultramicrotome sections. Allocation C2004,1,44,1,3 consisted of ten (27–36) of such serial sections that were placed on a 10 nm thick amorphous carbon film supported on a standard Cu TEM grid at NASA Johnson Space Center STARDUST Curatorial Facility. The analyses were performed using a JEOL 2010 high-resolution transmission electron microscope (HRTEM) that operated at a 200 keV accelerating voltage and was equipped with an ultrathin-window energy-dispersive X-ray detector for in situ quantitative chemical analyses, including oxygen, using the standard Cliff-Lorimer thin film procedure at UNM (see Zolensky et al. 2006, supplemental data). The analytical probe size (5, 10, or 15 nm) was selected to be always smaller than the object of interest. Phase identification was made by a combination of selected area electron diffraction (SAED) and energy dispersive spectroscope (EDS) data.

Allocation C2004,1,44,4,2 that was provided by NASA Johnson Space Center Stardust Curatorial Facility originated from grain #4 and consisted of eleven (16–26) serial ultramicrotome sections. The HRTEM analyses were performed at the University of Lille using a Tecnai FEI G2 operating at 200 kV equipped with an energy-dispersive X-ray spectrometer (EDS) detector. Correction procedures (*k*-factors and absorption corrections) were applied. The microanalyses were extracted from EDS X-ray elemental maps by summing the pixels of a spectrum image on areas of interest (see Zolensky et al. 2006, supplemental data).

OBSERVATIONS

Mineralogical Features: SXRD and Microtomography Analyses

Grain C2004,1,44,1,0

This grain measures 20 × 15 μm in size and appears to be an aggregate of silica aerogel and Wild 2 materials (Fig. 1a). It has an irregular surface with many aerogel fragments approximately 1 mm in size stuck to the surface. The SEM/EDS analyses show it contains a large amount of Si, moderate amounts of Mg, S, and Fe, and minor Ca, supporting chondritic abundances for these major-element abundances, except Si (Fig. 1b). The SXRD analysis shows only broad and no sharp reflections (Fig. 1c). The diffraction maxima are identified as suessite, Fe_3Si, and sulfide. Sulfide is either troilite (FeS) or pyrrhotite ($Fe_{1-x}S$), but these identifications are not conclusive because the sulfide diffraction peaks are too broad to distinguish the two minerals that give strongest lines at diffraction angles close to each other. We can distinguish suessite from kamacite on the basis of the diffraction angles (Fig. 1c). Suessite consistently yields

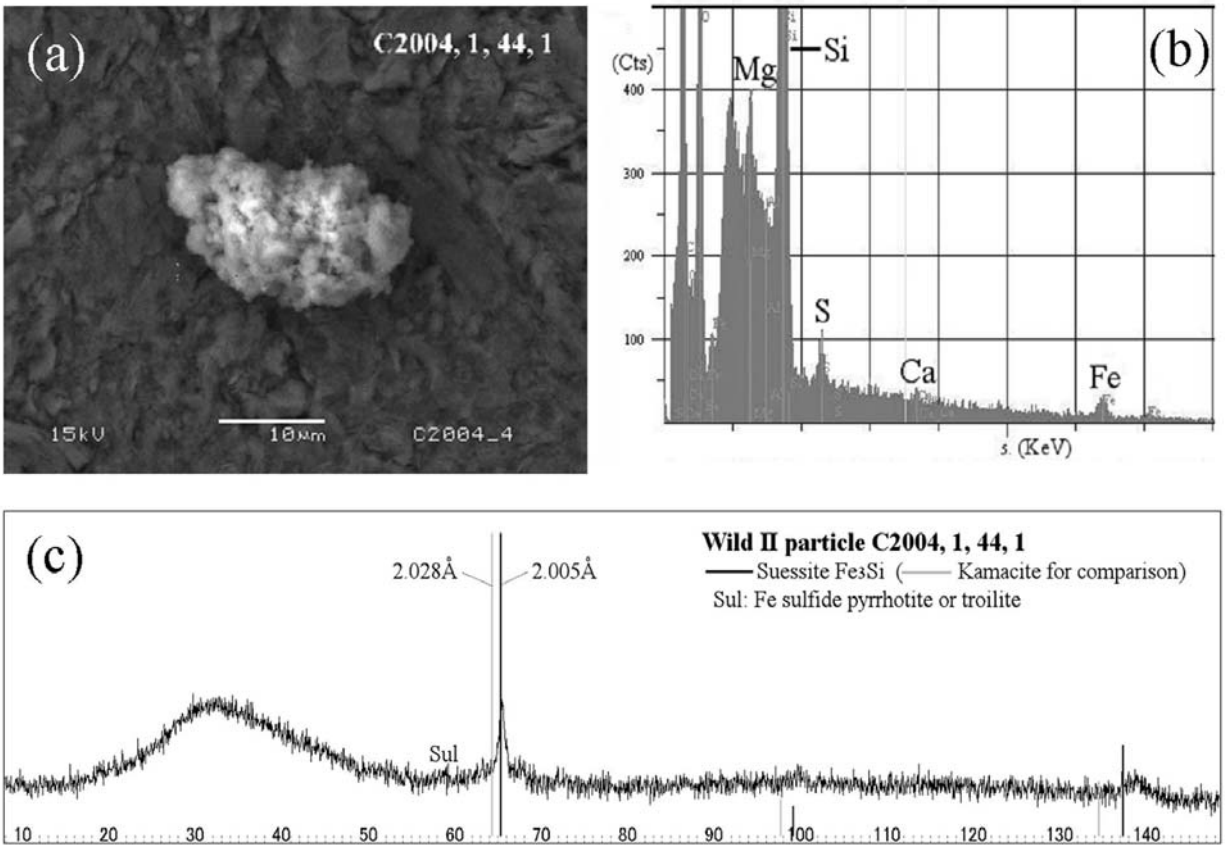

Fig. 1. Allocation C2004,1,44,1,0. a) The backscattered electron (BSE) image showing that the particle consists of gray (aerogel) and light materials (aerogel + Wild 2 materials). b) SEM/EDS spectrum showing a chondritic elemental pattern for Mg, S, Ca, and Fe, but not for Si, which includes an aerogel contribution. c) SXRD pattern showing very broad sulfide and suessite reflections. The peak center positions of kamacite are shown for comparison with suessite. Horizontal scale is 2θ diffraction angle and vertical one is arbitrary.

Table 1. Interlayer spacing, *d* (hkl) (Å) values and diffraction intensities of Fe-Si phases in allocations C2004,1,44,1,0, C2004,1,44,2,0, and C2004,1,44,3,0 compared to suessite (Keil et al. 1982) and kamacite (JCPDS 37–474).

(*hkl*)	*d* (Å)	C2004,1,44,1,0	C2004,1,44,2,0	C2004,1,44,3,0	Suessite[a]	Kamacite[b]
(110)	d	1.99	2.00	2.00	2.005	2.028
	Int[c]	100	100	100	100	100
(200)	*d*	1.41	1.41	1.41	1.420	1.434
	Int[c]	8	13	12	10	12
(211)	*d*	1.15	1.15	1.16	1.160	1.171
	Int[c]	40	33	29	30	18

[a]Keil et al. (1982).
[b]JCPDS #37–474.
[c]Integrated intensities are normalized to the (*110*) intensity and gave a 20% error.

diffraction peaks at angles higher than kamacite, since the suessite unit cell is smaller than kamacite by approximately 1% due to substitution of Fe by the smaller Si atom. The diffraction peaks for the Wild 2 allocations are almost identical to those of suessite (Fig. 1c). Table 1 shows that the integrated intensities for the diffraction peaks of suessite in the aerogel are comparable to those reported in literature (Keil et al. 1982).

Grain C2004,1,44,2,0

This grain, viewed in backscattered electron images, shows a melted material that is a mixture of silica aerogel and captured Wild 2 particulate matter (Fig. 2a). This allocated grain is also approximately 20 × 15 µm in size. SEM/EDS analysis also indicates similar chondritic elemental abundances as for C2004,1,44,1,0 (Fig. 2b). The SXRD patterns (Fig. 2c) are also very similar; only suessite and

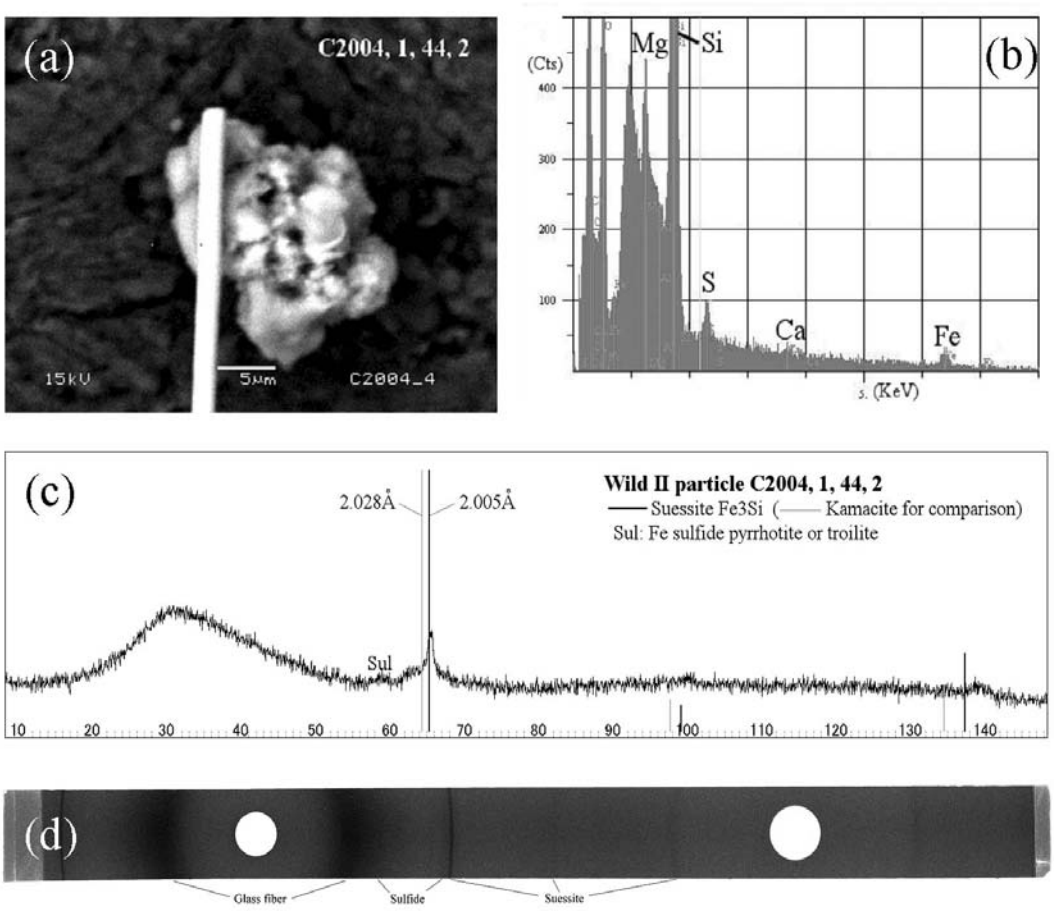

Fig. 2. Allocation C2004,1,44,2. a) The BSE image showing molten appearance. The rod attached to the particle is a glass fiber that holds particle during SXRD analysis. b) SEM/EDS spectrum showing a chondritic elemental pattern except for an enrichment of Si contributed by the aerogel. c) SXRD pattern that shows sulfide and suessite. Horizontal scale is 2θ diffraction angle and vertical one is arbitrary. d) Diffraction lines recorded on the imaging plate showing that the line of both sulfide and suessite are continuous and seamless circles.

sulfide were detected. The suessite diffraction characteristics in this grain are almost identical to those in C2004,1,44,1,0 (Table 1). The diffraction lines recorded on an imaging plate for both sulfide and suessite are continuous and seamless (Fig. 2d), indicating that both minerals occur as small polycrystalline grains, instead of large single crystal grains. While sulfide and Fe silicide phases were detected, no silicates were found by SXRD despite the presence of Mg in the EDS spectrum, suggesting that silicates are amorphous in this Wild 2 grain. A large, broad amorphous silicate peak was observed in the diffraction pattern at angles around 30 degrees (Fig. 2c). It is mostly generated from the 3 µm thick glass fiber supporting the grain.

Grain C2004,1,44,3,0

This grain is irregularly shaped and is 15 × 20 µm in size. Microtomography shows a porous material with numerous voids that are mostly <1 µm in size, a few large voids (3–4 mm), and a three-dimensional network of fine-grained materials probably made of melted aerogel, silicates, sulfides, and suessite (Figs. 3a–c). The presence of abundant voids (~56 vol% porosity) might support melting, devolatilization, and rapid cooling. The surface is irregular and resembles the other two grains (Fig. 3d). SXRD analysis shows suessite and sulfide as the only crystalline phases present (Fig. 3e). Based on the 3-D CT images, the mode of suessite and sulfide phases is approximately 0.06 vol% (Fig. 3d). The maximum size of these individual phases is about 700 nm and most are <300 nm. These sizes are larger than those observed for these phases in grain C2004,1,44,1,0; see the HRTEM and ATEM Analyses of Allocation C2004,1,44,1,3 section below. The apparent different findings may be due to 1) similar size distributions, but large grains were not observed by HRTEM, 2) overestimation of grain size by CT due to inadequate threshold to extract the Fe-Si and Fe-Ni-S phases, or 3) inherently different size distribution in the allocations. The similarities among this grain's shape and SXRD pattern to the other two grains described above suggest that all three have similar internal structures and all three grains are very porous.

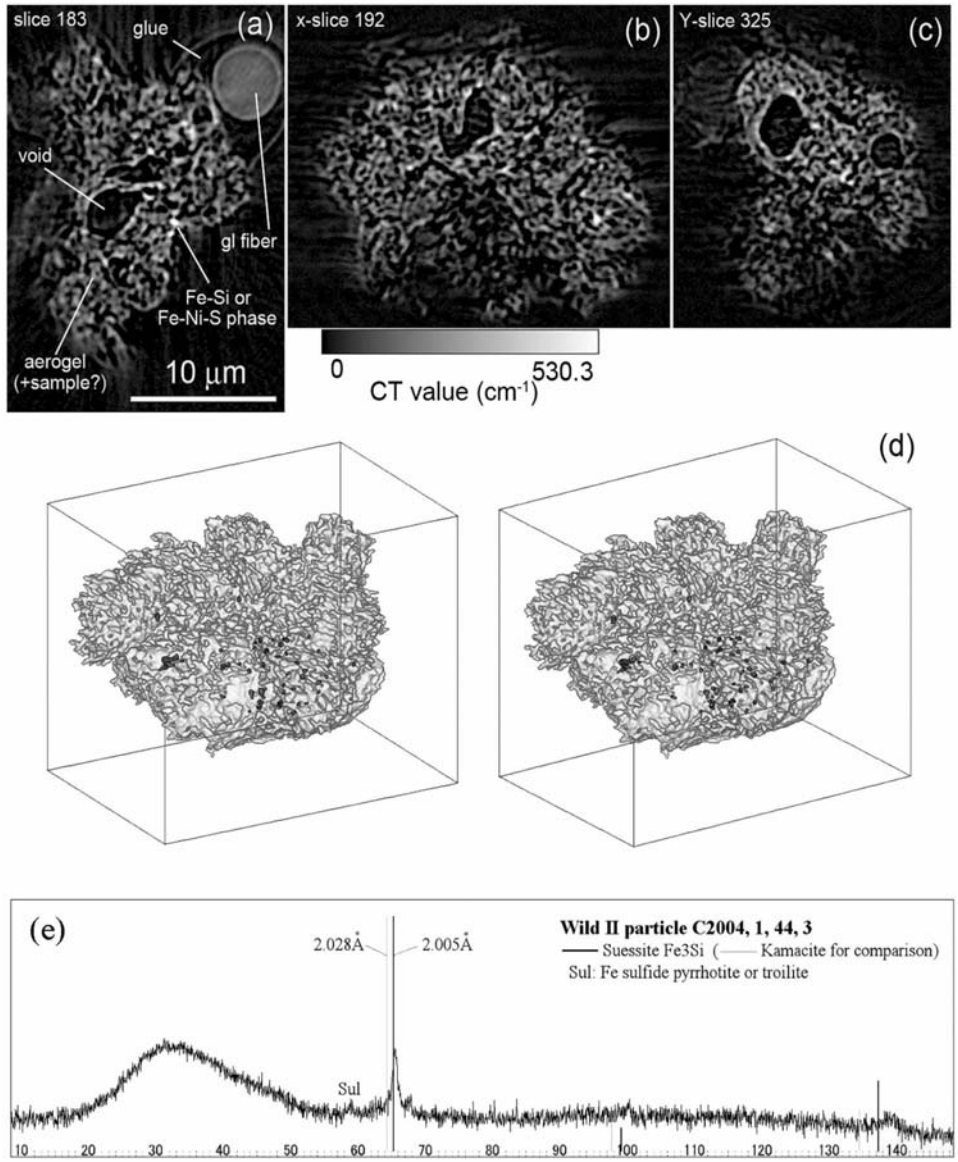

Fig. 3. Allocation C2004,1,44,3,0. a) Microtomography image of a cross section showing the many voids in this grain and the network of light-colored material. b) Sequential CT images through the grain from top to bottom showing the omnipresent small voids; (b) is a cross section oriented vertical to (a). c) A cross section oriented perpendicular to the (a) and (b) images. Scale bars and grayscale are identical in all three images. d) Stereographic images of the external shape of the sample (box size = 17.8 × 26.1 × 20.2 mm) composed from the 3-D CT images. Small grains of highly absorbing phases (red) might correspond to the Fe-Si or Fe-Ni-S phases dispersed in the sample interior; no large grains were found. e) SXRD pattern of entire grain C2004,1,44,3,0. Horizontal scale is the 2θ diffraction angle; vertical scale is arbitrary.

HRTEM and ATEM Analyses of Allocation C2004,1,44,1,3

The ultrathin sections in this allocation show mostly massive aerogel, occasionally with few tiny vesicles, intermingled with areas of vesicular aerogel that also incorporate rare GEMS-like spheres (cf. Zolensky et al. 2006). While in this paper we use the term "massive aerogel," Leroux et al. (2008) refer to the same material as silica or Si-rich glass. Electron-opaque inclusions abound ranging from a few nanometers up to several tens of nanometers. Massive aerogel contains areas with only very few, typically the tiniest, inclusions. Most common is a "shotgun pattern" of larger, mostly spherical inclusions in vesicular aerogel (Fig. 4) that is common in Stardust aerogel investigated so far and they include pyrrhotite and/or troilite, low-S Fe-Ni-S phases, and Fe(Ni) metal (Zolensky et al. 2006; Leroux et al. 2008). The smallest inclusions range from 3 nm to 14 nm when aerogel is still mostly "clean" stoichiometric SiO_2. Quantitative analysis of these inclusions is unreliable at best, but it is not the case for opaque inclusions with diameters approaching or larger than

Table 2. Fe-Ni-S phases as a function of increasing sulfur content that form two populations (low and intermediate values) and four polycrystalline mineral grains with high-S content.

	Very low		Intermediate	High	
wt%					
Fe	93.2	86.3	74.6	67.1	55.7
Ni	5.4	2.2	1.85	0	0
S	1.3	11.5	23.5	32.9	44.3
at%					
Fe	92.6 (88.7–97.6)	79.6 (62.8–89.9)	63.6	52.3	47.5
Ni	5.1 (0–8.4)	1.95 (0–5.0)	1.5	0	0
S	2.3 (1.0–4.2)	18.4 (8.2–35.7)	34.9	44.7	52.5
Grain size (nm)	20–100 (57)	14–50	126 × 104; 87 × 75	150 × 150	67 × 43

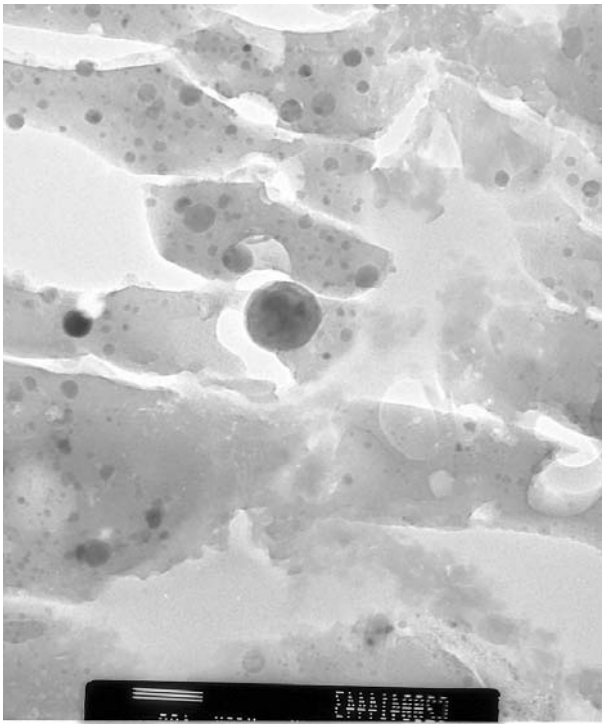

Fig. 4. Low-magnification, transmission electron microscope image of typical aerogel with scattered round inclusions of Fe-Ni-S phases with widely variable diameters in allocation C2004,1,44,1,3 embedded in epoxy (light gray area). Aerogel shows shattered fracturing behavior during ultrathin section preparation that would be consistent with a quenched-melt glass-like material. The circular embayment and other, highly transparent circular features are large vesicles in aerogel. The scale bar is 50 nm.

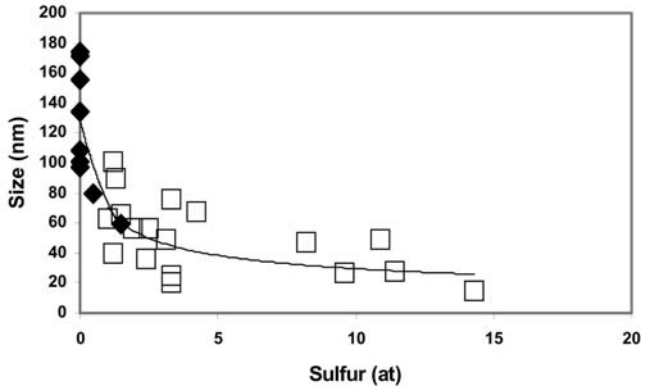

Fig. 5. Sulfur content of inclusions S < 15 at% (open squares) and S = 0 (solid diamonds) in aerogel as a function of size (nanometer). The S-free phases contain no oxygen. When the analytical probe is moved off these phases onto the aerogel, oxygen is detected from the SiO_2 aerogel.

the section thickness. In vesicular aerogel, the inclusions are larger on average (up to ~60 nm) with a few inclusions that are larger still (up to ~100 nm). Vesicular aerogel typically contains trace to minor amounts of Fe and S and Mg. Sections 27–29 contain a regularly shaped, 390 × 270 nm, olivine single crystal ($Fo_{98}Fa_2$), but it not clear that it was the source of Mg found in the aerogel (Leroux et al. 2008).

There is a great abundance of Fe-Ni-S phases with a wide range of S-content and grain size (Table 2). They include an elongated, 67 × 43 nm, single-crystal (SAED) of Ni-free pyrrhotite (S = 52.5 atomic; $Fe_{0.9}S$). Other high-S phases (Table 2) include single-crystal pyrrhotite (S = 44.7 at) with a superimposed single-crystal SAED kamacite pattern. The small numbers for the high-S phases have no statistical relevance, but indicate they are rare compared to the Fe-Ni-S phases of the other two groups. Phases with intermediate sulfur content typically produced SAED patterns with strong scattered maxima for a pyrrhotite phase plus a much weaker scatter pattern for small kamacite crystals. These phases are random intergrowths of fine-grained sulfide and metal crystals. The low-S group of typically spherical kamacite is remarkable only for its high Ni-content. All Fe-Ni-S phases contain chromium ranging from 0.2 to 1.5 (at) with an average of 0.95 Cr (at). One low-S phase contained 2.6 at% Cr. There is no correlation between the Cr and Ni (at) contents. Another allocation (C2004,1,44,4,4) from track #44 had a high density of almost pure Fe-(Ni) kamacite crystals (Tomeoka, personal communication, 2006).

The size-composition (S atomic) relationships are anti-correlated (Fig. 5). The sizes for the mostly spherical (and rare elongated spherical) grains with neither S nor O (Fig. 5) are shown in Table 3 along with the only euhedral grain.

Table 3. Compositions of eight Fe-Si phases in allocation C2004,1,44,1,3 from track 44 in cell C2004.

	Fe-Si phases								Fe_3Si Suessite[a]		Fe_2Si
	#1	#2	#3	#4	#5	#6	#7	#8	Low-Ni	High-Ni	Hapkeite[b]
wt%											
Fe	73.9	74.2	78.9	79.2	80.8	81.4	82.2	83.1	84.7	83.1	75.3
Si	20.9	20.4	12.8	15.3	13.4	13.2	14.6	12.4	15.3	13.7	18.4
Co	n.d.	n.d.	n.d.	n.d.	n.d.	n.d.	n.d.	n.d.	0.21	0.27	0.12
Ni	4.2	4.2	6.1	4.5	5.2	4.4	2.0	3.3	1.6	4.5	3.14
P	n.d.	n.d.	n.d.	n.d.	n.d.	n.d.	n.d.	n.d.	0.06	0.17	1.85
Cr	1.0	1.2	2.2	1.0	0.5	0.9	1.2	1.1	0.10	0.04	0.37
Total	100	100	100	100	99.9	99.9	100	99.9	101.97	101.78	99.2
at%											
Fe	61.3	61.1	70.1	68.7	71.4	72.1	71.9	73.8	72.3[c]	72.1[c]	63.4
Si	34.5	33.4	22.6	26.3	23.6	23.3	25.3	22.0	26.0	23.6	30.8
Co	n.d.	n.d.	n.d.	n.d.	n.d.	n.d.	n.d.	n.d.	0.17	0.22	0.09
Ni	3.3	3.3	5.2	4.1	4.4	3.7	1.7	2.8	1.3	3.7	2.51
P	n.d.	n.d.	n.d.	n.d.	n.d.	n.d.	n.d.	n.d.	0.09	0.27	2.82
Cr	0.9	1.1	2.1	0.9	0.5	0.9	1.1	1.0	0.09	0.03	0.33
Total	100.0	98.9	100	100	99.9	100	100	99.6	99.95	99.92	100

[a]Keil et al. (1982).
[b]Anand et al. (2004).
[c]Calculated by the present authors.

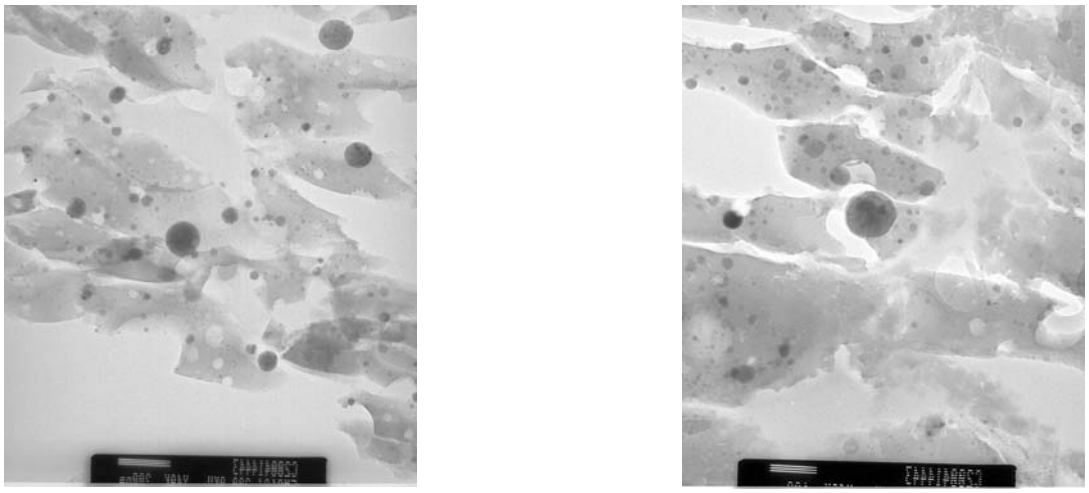

Fig. 6. Low-magnification, transmission electron microscope image allocation C2004,1,44,1,3 showing the highly shattered aerogel embedded in epoxy (light gray) with numerous small vesicles and scattered Fe-Ni-S spheres. (a) Two large spheres in the lower left hand part of this image and the large sphere close to its center are iron-silicide spheres. The mottled (back speckles) texture visible in the spheres to the left is consistent nanocrystals forming in the quenched-melt Fe silicide spheres. The scale bar is 200 nm. (b) The large iron-silicide with its mottled texture is associated with an area of shattered and vesicular aerogel that has a high concentration of Fe-Ni-S phases. It appears that both the number and sizes of these Fe-Ni-S spheres decease towards to Fe silicide phase perhaps supporting the notion that iron for the large silicide sphere was extracted from surrounding Fe-Ni-S phases. The scale bar is 100 nm.

Although there is some overlap, they are mostly larger than the Fe-Ni-S phases with low sulfur content.

The Fe-Si phases include one euhedral grain (123 nm × 52 nm), five spherical grains, and two slightly elongated spheres. They show a range of Fe/Si ratios and contain Cr (0.9–2.2 el%) and Ni (2.0–6.1 el%) (Table 3). The (sub)-spherical grains range from 79 to 140 nm, averaging of 112 nm in diameter. Their mottled texture due to electron-opaque inclusions ~2 nm to ~7 nm in size suggests they could be intimate intergrowths of two or more phases (Fig. 6). The Fe-Si phase compositions in the aerogel match the hapkeite and suessite compositions (Table 3), but most contain more iron (Fig. 7). They are the most Fe-rich Fe-Si phases yet reported.

The Fe-Si phase SAED data match those for iron silicides (Table 4). The single-crystal SAED patterns of these phases in

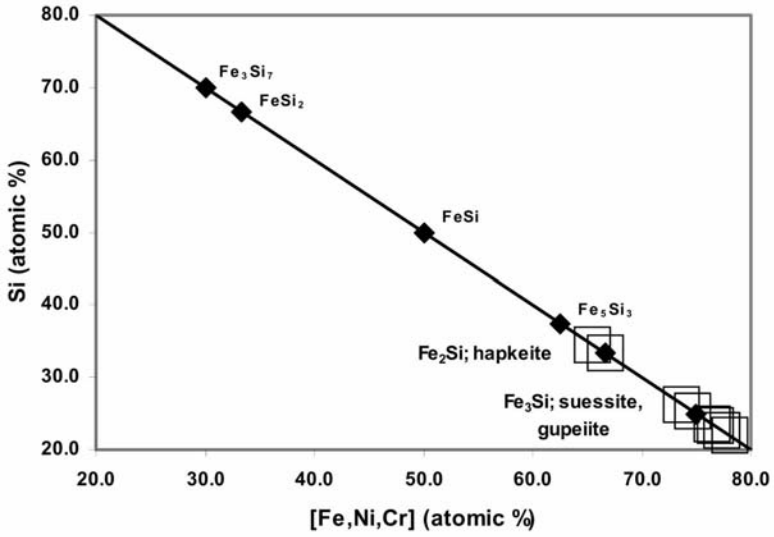

Fig. 7. Compositions of Fe-Si phases in aerogel (open squares) compared to naturally occurring Fe silicide phases (solid diamonds): Fe_3Si_7 (Essene and Fischer 1986), $FeSi_2$ (Anand et al. 2004), FeSi (Anand et al. 2004; Essene and Fischer 1986), Fe_5Si_3 (Yu 1984), Fe_2Si (Anand et al. 2004), and Fe_3Si (Keil et al. 1982).

aerogel are generally accompanied by a single-crystal pattern of distinctly finer (weaker) maxima. Based on two interlayer values, viz. $d = 0.31$ nm [*hkl*: 220 (kamacite)] and $d = 0.47$ nm [*hkl*: 200 (kamacite)], this phase could be kamacite. The mottled texture of the Fe-Si spheres suggests the presence of two mineral species. The data shown in this table also support the presence of two different minerals, Fe-Si phases and kamacite, but as hapkeite (Anand et al. 2004) and suessite (Keil et al. 1982) both have a kamacite structure, we cannot distinguish a mixture of two Fe-Si phases or an intergrowth of Fe-Si with iron metal.

Keil et al. (1982) defined low-Ni (0.5–2.4 wt%) and high-Ni (2.9–6.4 wt%) suessite, which means that the Fe-Si phases in aerogel are high-Ni phases, with one exception. They contain more Cr than the meteoritic and lunar iron silicides (Table 3), but have no detectable Co and phosphorous. Gupeiite (Fe_3Si) contains minor amounts of Mn and Ni (Xu 1984). The silicide composition in aerogel could contribute to a slightly larger unit cell, which seems to be borne out by their *d*-values, which are slightly higher than those for natural silicides (Table 4). The SAED data for the third Fe-Si phase, which has the highest Ni content, in the aerogel match well with gupeiite $(Fe_{2.97}Ni_{0.03}Mn_{0.02})(Si)_{0.98}$; Yu 1984), which has twice the unit cell (f.c.c. cubic, a_0 = 5.67 Å; Yu 1984) than other Fe_3Si minerals (b.c.c. cubic, a_0 = 2.84 Å; Keil et al. 1982) (Table 4). Keil et al. (1982) noted that suessite $[(Fe_{2.87}Ni_{0.08}Co_{0.008}Cr_{0.004})(Si,P)_{1.0}]$ might be a solid solution in the Fe-Si system rather than a perfect Fe_3Si albeit, but that the latter cannot be ruled out. From their data, we extrapolate that while crystallographic, discrete Fe-Si alloys will exist, each phase has a certain chemical variability relative to its stoichiometric composition.

HRTEM Element Mapping of Allocation C2004,1,44,4,2

The ultrathin sections of this allocation show identical features as described above for allocation C2004,1,44,1,3, but most of the opaque inclusions are S-poor Fe-S spheres (Leroux et al. 2008), while sulfur seems to be evenly distributed in the glass matrix. Often irregular pyrrhotite is present as relatively large grains (Leroux et al. 2008). The elemental distributions for Si, O, and Fe, including a map of the "Si-O" difference to enhance the presence of Si, reveal other spheres in this allocation that are Fe silicide (Fig. 8). They are between 50 and 100 nm in diameter. Their compositions (Table 5) are indistinguishable from those in the other allocation from track #44 that were obtained by focused electron beam EDS analysis (cf. Table 3).

DISCUSSION

Combining composition and crystallographic properties the mostly Ni- and Cr-bearing Fe-Si spheres scattered within the silica aerogel capture medium of Stardust were identified as iron silicides, including hapkeite and suessite, but also silicides with much higher Fe/Si ratios. Based on the unit cell data for previously reported Fe silicides, we feel confident of our identification of Fe silicides in the aerogel. Suessite was found in three grains from track #44 and in more than ten grains from track #35 (Nakamura et al. 2008). All suessite-containing grains were recovered from the walls of the tracks. Although only one suessite-containing grain was investigated by microtomography, it shows clear evidence of melting and mixing of silica aerogel and Wild 2 materials at the 10 to 20 μm scale. Suessite-containing grains are rich in Mg,Si-rich amorphous materials.

Table 4. Interplanar spacings, *d* (*hkl*) (Å), based on SAED diffraction analyses for (Fe,Ni,Cr)Si phases in aerogel of track #44 (allocation C2004,1,44,1,3) compared to hapkeite, synthetic iron silicide, suessite, the intermetallic compound Fe_3Si (BiF_3-type) and gupeiite. The (*hkl*) indices for kamacite with ~6.6% Ni for are shown in italics. The gupeiite unit cell is twice the unit cell of other Fe silicides for which the (*hkl*) indices are bold highlighted.[a]

	C2004,1,44,1,3			Fe_2Si			Fe_3Si		
(*hkl*)	1	2	3	Hapkeite[b]	Synthetic[c]	Suessite[d]	BiF_3[d]	Gupeiite[e]	Kamacite[f]
(100)									8.60
(100)								5.67	
(200)									4.495
(210)			3.96						3.85
(112)			3.50						3.51
(111)		3.19					3.26	3.26	
(220)									3.03
(221)		2.95							2.95
(200)								2.83	
(100)	2.83		2.84	2.83	2.82	2.84	2.82		
(320)									2.455
(321)									2.23
(400)									2.12
(322)									2.10
(330/441)		2.05							2.03
(220)								2.00	
(110)	2.00		2.00	2.00	1.99	2.005	1.99		
(331)									1.98
(311)			1.86				1.70	1.71	
(222)								1.63	
(111)				1.63	1.615				
(?)			1.50						
(400)								1.415	
(200)		1.47	1.42	1.415	1.41	1.42	1.41		
(331)			1.30					1.30	
(210)			1.27	1.27	1.26				
(422)							1.15	1.16	
(211)	1.16		1.13	1.155	1.15	1.16			
(511)			1.04					1.09	
(440)								1.00	
(220)			0.98	1.00	0.995				

[a]The kamacite (*210*) and (*112*) values were calculated by the present authors. The *d*-values for Fe-Si phases in the aerogel have a 5–10% relative error.
[b]Data from Anand et al. (2004).
[c]Data from Khalaff and Schubert (1974).
[d]Data from Keil et al. (1982).
[e]Data from Yu (1984).
[f]JCPDS #18–645.

Table 5. Compositions (atomic%) for ten Fe-Si phases in allocation C2004,1,44,4,2 from track 44 in cell C2004.[a]

	#9	#10	#11	#12	#13	#14	#15	#16	#17	#18
at%										
Fe	58.5	61.7	66.0	70.6	72.3	72.7	73.1	74.8	79.3	79.5
Si	40.2	27.2	26.7	23.8	21.4	21.5	25.6	20.7	14.8	14.6
Ni	0.7	9.1	4.7	4.3	4.1	4.5	0.9	3.4	4.3	5.0
Cr	0.5	2.0	2.6	1.1	2.3	1.3	0.4	1.1	1.5	0.8
Total	99.9	100.0	100.0	99.8	100.1	100.0	100.0	100.0	100.9	99.9

[a]Co and P were not detected. Individual size data for these Fe silicide spheres are unavailable, but they are all <100 nm in diameter.

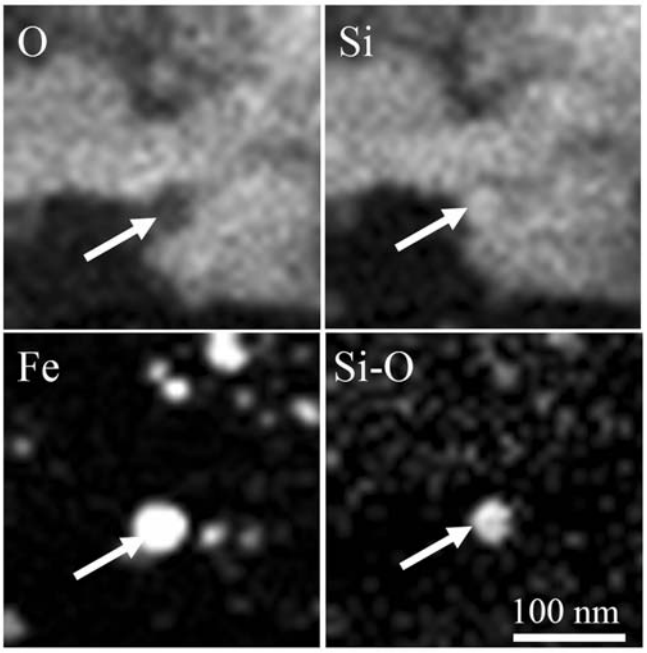

Fig. 8. X-ray intensity maps for Si, O, and Fe in allocation C2004,1,44,4,2. The Si-O image shows the subtraction of the O intensity from the Si intensity, which visually emphasizes the presence of Si in the Fe-rich spheres. This figure shows an example of the Fe-Si spheres (arrows) in this allocation. The much smaller spheres are probably Fe spheres, although we cannot entirely exclude the possibility that some of these could be Fe silicides.

The Fe silicide phases formed near the entrance of track #44 and this very location might well bear on their presence, but what can we infer about their origins from their compositions? Iron silicides produced by a lightning strike contain no Ni and Cr (Esssene and Fischer 1986), which reflects the local soil composition, as in general, terrestrial soils have very low Ni and Cr contents. The meteoritic and lunar Fe silicides contain Ni (Keil et al. 1982; Anand et al. 2004) that is expected because of the low cosmic Fe/Ni ratio compared to this ratio for terrestrial rocks (cf. Rietmeijer 1998). The high Ni contents of Fe silicides in the aerogel suggest they or their precursors are debris from comet Wild 2. Their Ni contents, 1.7–5.2 (at), are similar to the Ni contents of 1–8 (at) in low-S Fe-Ni-S phases in the aerogel. They contain 0.5 to 2.1 Cr (at). The Fe-Ni-S phases contain between zero and 1.5 at%, with an average Cr = 0.9 (at). These similar Ni and Cr contents of Fe-Ni-S and Fe-Si phases in the aerogel strongly suggest a genetic link.

The reported Fe silicide occurrences include 1) blebs to elongated grains ranging from 1 μm to 150 × 30 μm as vein fillings in silicates and carbonaceous material in a highly shocked ureilite (Keil et al. 1982), 2) 2–30 μm size grains in lunar regolith breccia clasts due to space weathering (Anand et al. 2004), 3) melt inclusions (<25 μm) in silica-rich fulgurite glass due to a lightning strike in terrestrial soil (Essene and Fischer 1986; Ramírez-Cardona et al. 2006), and 4) hypervelocity impact structures (Rowan and Ahrens 1994). Gupeiite and xifengite, surrounded by nickel-iron minerals and their oxidation products, are found at the core of spheres found in placers in the Yanshan Mountains (China) that appear to be meteor ablation spheres (Yu 1984).

Iron silicides in lightning strike fulgurites were produced during extreme melting and metal-silicate liquid immiscibility at reducing conditions due to carbonaceous matter present above ~2300 °C of the SiO_2-Si buffer, viz. $fO_2 = 10^{-20}$ (1873 °C) to 10^{-15} (2273 °C) with Si metal present at 1923–2200 °C (1 mole SiO_2; 0.25 moles C at 1 bar pressure) (Essene and Fischer 1986; Wasserman et al. 2002; Ramírez-Cardona et al. 2006). Models for fulgurite formation and hypervelocity impact processes conclude that high-temperature reduction of silicates and chemical reduction of SiO_2 between 3100 °C and 4873 °C produced metal-silicate melts and vapor due to the thermodynamic instability of oxides well above 2800 °C at 1 atm. (Badjukov and Petrova 1992; Rowan and Ahrens 1994; Wasserman and Melosh 2001; Sheffer et al. 2003; Jones et al. 2005). These models do not invoke buffered reducing conditions. Keil et al. (1982) attributed suessite in the North Haig ureilite to "extreme" shock levels and regimes of rapidly increasing and rapidly falling temperatures causing the reduction of Fe in Mg,Fe olivine by reactions with carbonaceous material and the formation of Si and Fe melts in part also from co-existing kamacite. Melting and vaporization of lunar surface soil due to hypervelocity meteorite and micrometeorite impacts, and cosmic ray and solar wind particle exposure caused gas molecule dissociation well above 2400 °C (Anand et al. 2004). These proposed formation mechanisms show considerable communality of the conditions required to form Fe silicides.

Based on this information, the prerequisites for Fe-Si formation are summarized as follows:

1. Source(s) for Fe and Si; iron was available from collected Wild 2 dust while the aerogel capture medium was an ample source of Si.
2. Extreme reducing conditions; conditions such as could be induced by carbon, nitrogen, or hydrogen cannot be assessed at this time. Carbonaceous matter in aerogel was present from comet Wild 2 (Sandford et al. 2006) and spurious terrestrial matter. Its presence might have decreased fO_2 in melted grains, if only on very localized scales, thus promoting SiO_2 reduction.
3. Very high heating rates to high temperatures, probably well above 1700 °C, that will depend on the aerogel response to the hypervelocity impact (Anderson and Ahrens 1994).
4. Very high cooling rates.

The Fe silicides formed near the top of the track caused by a hypervelocity impact that quickly generated extreme high temperatures near the track entrance. The proximity to the space environment perhaps partially ensured that the second and third requirements were no limiting factors even in the

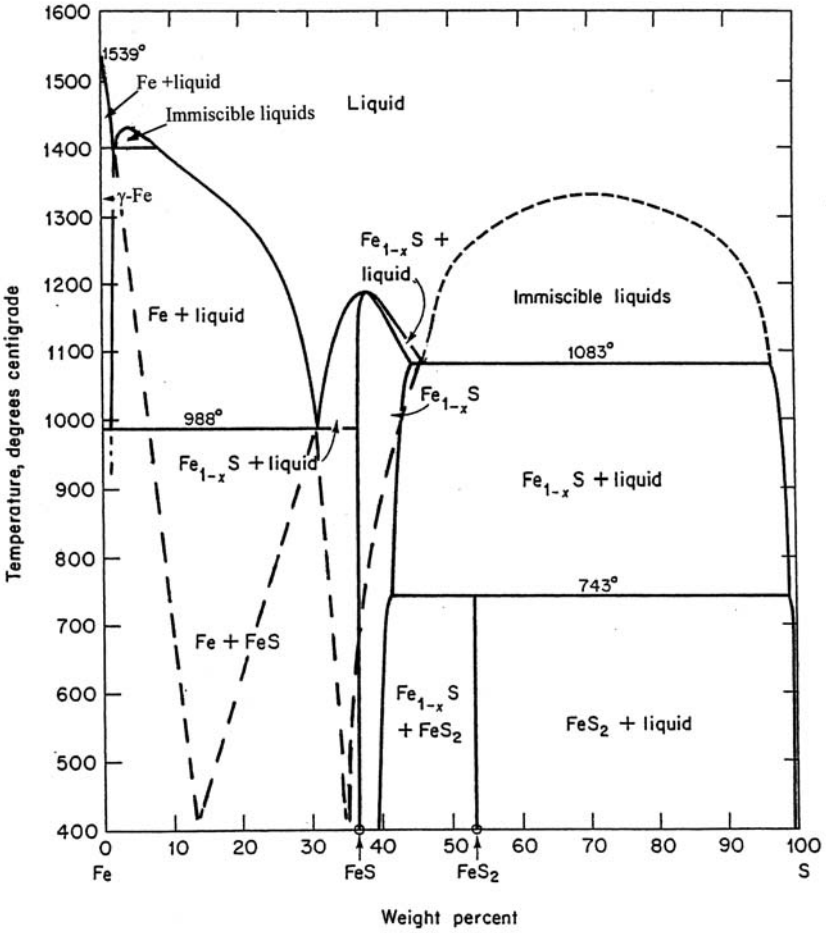

Fig. 9. Fe-S (wt%) phase diagram (modified after Kullerud et al. [1969]) incorporating the experimental data from Wever (1928) and Hansen (1958) at low-S compositions. The modified diagram has an additional eutectic composition very close to the pure Fe side of the diagram. The dashed lines show the deep metastable eutectics that are possible as a result from the proposed modification. While the Fe/S ratios of the DMEs are constrained, the temperatures at which they occur are not. Their positions indicated just above 400 °C are fortuitous and are not necessarily their actual formation temperature in the Stardust mission aerogel.

absence of chemical reducing agents. Also, very high quenching rates would be more likely at the top of a track than deeper into the aerogel. Qualitatively at least, it appears that the conditions existed to produce Fe silicides as a consequence of hypervelocity impact capture of Wild 2 debris.

The Fe-Si phases in aerogel include Fe_2Si and Fe_3Si, but most of them are more Fe-rich. The most Fe-rich silicide (Table 3, #8), $(Fe_{3.35}Ni_{0.13}Cr_{0.05})(Si)_{1.0}$, has the ideal structural formula Fe_7Si_2, which might be an as-yet unnamed Fe-rich, (Fe,Ni,Cr)Si alloy. An Fe silicide phase with the same Fe,Si composition was found in hypervelocity impact experiments of metal projectiles into silicate minerals that produced melt spheres of very high-iron, Si-Fe phases (Badjukov and Petrova 1992). They did not report details of the experimental conditions and crystallographic properties of the Fe-Si phases. Their work lends support that extreme high-temperature reduction was involved in the formation of Fe silicides in the Stardust mission's aerogel in a process that involved first melting and reduction of SiO_2 aerogel and then intimate mixing of Wild 2 dust and melted silica aerogel that would probably suppress olivine crystallization but instead favor the formation of a glass phase.

The highly kinetic physiochemical conditions leading to the formation of Fe silicides associated with the hypervelocity impact of a Wild 2 particle that probably contained (Fe,Ni)-sulfides, since troilite and/or pyrrhotite minerals one micron and larger in size (Zolensky et al. 2006) are found in aerogel, were not conducive for reactions proceeding at thermodynamic equilibrium. Still, the Fe-S (wt%) phase diagram (Kullerud et al. 1969) may serve as a guideline to trace the development of phase relationships that might have existed, but in the following, we ignore any effects that could arise from Ni and/or Cr in the Fe-Ni-S and Fe-Si phases.

The anti-correlated grain size and S contents are expected for melting of an Fe-S phase to above the eutectic temperature at 988 °C when Fe + FeS is in equilibrium with Fe + Liq and

$Fe_{1-x}S$ + Liq to slightly above 1500 °C (Kullerud et al. 1969). Aerogel is riddled with inclusions of sub-S sulfide compositions (Zolensky et al. 2006) that, we submit, could represent quenched liquids of Fe.FeS compositions at ~30 sulfur (wt%) between pure Fe and the Fe-S eutectic. Aerogel melts around 1200 °C and molten silica could have reacted with a close to eutectic $FeS_{0.5}$ (S = 33 at) composition to yield droplets of Fe silicide melts:

$$0.5(Fe.FeS)_{liq} + (SiO_2)_{liq} = FeSi_{liq} + (^{8+}S_{0.5}O_2)_{vapor} \quad (1)$$

and, for example, for suessite,

$$1.5(Fe.FeS)_{liq} + (SiO_2)_{liq} = Fe_3Si_{liq} + [^{4+}S_{0.5}O + (SO]_{vapor} \quad (2)$$

The fate and gas molecule speciation of the resulting vapor is unknown but sulfur "hotspots" with a different isotopic signature than the precursor Fe-Ni-S phases and sulfide minerals should be present in aerogel, assuming the vapors have not escaped into space. With increasing temperatures and for increasingly more Fe-rich Fe.FeS liquids, increasingly less SO gas will be produced. Finally, when a pure iron melt reacts with molten SiO_2, the only gas species will be oxygen and its presence will inhibit Fe-Si phase formation as quenched melt products. The temperatures in this argument would have existed had the entire process occurred at thermodynamic equilibrium, but we do not yet know how much higher peak temperatures might have been during hypervelocity impact of the Wild 2 particles. Computer modeling studies indicate temperatures as high as 10,000 °C could be generated (Anderson and Ahrens 1994).

When temperatures were indeed in excess of those based on phase equilibrium, silicide formation might have transited into a regime of extreme disorder of the type encountered for dust condensation in silicate vapors under laboratory conditions but that also simulated fulgurite analog formation (Rietmeijer et al. 1999a, 2000). Under these kinetic conditions, solids with predictable deep metastable eutectic compositions formed in preference of the thermodynamically stable minerals.

The Fe-S (wt%) phase diagram (Kullerud et al. 1969) is a composite of the binary systems Fe-FeS and FeS-S, which is important to unravel the behavior of Fe-Ni-S phases that were the precursors to the Fe silicides in track #44. The sulfide compositions at Fe/(Fe + S) is 0.44 and 0.33 (Table 2) coincide with the eutectic compositions on either side of the $Fe_{1-x}S$ + liquid fields. It strongly points to FeS sulfide (cf. Zolensky et al. 2006), as the precursor for the observed phases when it was heated above its meting point at 1200 °C (Fig. 9). For reference, the Fe-Ni-S phase compositions at Fe/(Fe + S) at 0.24 and 0.115 (Table 2) would when at equilibrium indicate a temperature of about 1400 °C, but since equilibrium was probably not achieved, the actual temperatures could have been higher (Anderson and Ahrens 1994). Aerogel was initially transformed to a high-density amorphous phase that melted upon pressure release, implying that (Fe,S) melts were most likely achieved.

The very low sulfur contents of the Fe-Ni-S phases (Table 2) are not constrained by the current Fe-S phase diagram. We submit a modification of this existing phase diagram to allow these phases to be defined. That is, instead of a flexure in the surface of the Fe + Liq field, there is an Fe-rich two-liquid field and a eutectic at S = 1.5 (wt%; calculated on a Ni-free basis) and 1381 °C (the γ-Fe melting temperature) for a γ-Fe field that in this modification terminates at 988 °C (Fig. 9). The iron phase that is identified in the existing diagram will be α-Fe. Although it is beyond the scope of this paper, we highlight two issues that will need to be addressed, viz. 1) the γ-Fe to α-Fe transition occurs at 912 °C, and 2) the contracted γ-Fe field as shown might be an expanded field as discussed by Wever (1928) and Hansen (1958). In either case, the current phase diagram requires adjustments near the Fe metal phase below 1000 °C, although the exact phase fields remain to be established. With this modification, there are two deep metastable eutectics (cf. Nuth et al. 1999, 2002; Rietmeijer and Karner 1999; Rietmeijer et al. 1999b, 2002) in this phase diagram located between 10–20 wt% and 30–40 wt% sulfur shown at S = 12 wt% (cf. Table 2) and close to the FeS composition (Fig. 9). We submit that the quenched-melt Fe,S droplets that formed during hypervelocity impact of Wild 2 material matched either one of the two DME compositions. The corollary of this behavior will be 1) solids with an FeS can be quenched-melt phases among surviving FeS sulfides, and 2) the iron content of the intermediate sulfur containing Fe-Ni-S phases is fixed at the DME composition at Fe = 81 at%. This value is close to Fe/(Fe + Si) = 0.77 for the most Fe-rich silicide in the aerogel (Tables 3 and 5). When Fe phases in the Fe-S (el) phase diagram cause a eutectic close to the Fe endmember, then the same situation could arise in the Fe-Si phase diagram (Hansen 1958). When such a eutectic point is accepted, there will be deep metastable eutectic between 10–15 Si (at) or ~7 Si (el). This DME composition matches the aerogel Fe_7Si_2 silicide (Tables 3 and 5).

Formation of Fe silicides from this DME Fe-Ni-S phase is essentially an exchange of S for Si when melted aerogel in the reaction has lost its oxygen. Assuming the vapor molecule was the stable SiO gas phase molecule (Nuth and Donn 1982), the reaction was:

$$Fe_4S_{(liquid)} + SiO_{(liquid)} = Fe_4Si_{(solid)} + SO_{(vapor/liquid)} \quad (3)$$

Of course, when dissociation of gas phase molecules in a vapor produced by the hypervelocity impact yielded Fe^0 and Si^0, none of the above scenarios could apply. A role of a vapor in the formation of the massive Fe silicide spheres was unlikely considering their size, which is more consistent with melt formation (Rietmeijer et al. 1999b).

The subsequent regime of falling temperature occurred in aerogel, which is a perfect thermal insulator and which was at

least slow enough for (partial) subsolidus annealing of the Fe-Ni-S and Fe silicates, which is indicated by diffraction data for the quenched-melt spheres, typically showing two crystalline phases. We stress the nanometer scales of extreme but variable intensity—heating that existed when scattered Fe silicides formed by interactions between Wild 2 sulfides and silica aerogel. At this time, no generalizations of peak temperatures during Wild 2 dust capture can be inferred, but minimum temperatures are implied.

CONCLUSIONS

Quenched-melt iron silicide spheres with hapkeite, suessite, and up to Fe_7Si_2 compositions are mixtures of nanocrystalline Fe-Si phases and kamacite that were formed during hypervelocity impact of the Wild 2 particle that caused track #44 of the aerogel collector. The data support a formation whereby melted Fe-Ni-S material from the comet could react with melted aerogel. When formed under conditions conducive to thermodynamic equilibrium, temperatures were probably around 1500 °C, but higher aerogel temperature were more likely. In that case, the phase relations among the Fe-Ni-S phases and the newly formed Fe-Si phases might have shown deep metastable eutectic behavior such as observed in laboratory condensation experiments and in terrestrial process of both ultra-rapid heating and cooling rates.

Acknowledgments–We thank Don Brownlee and Mike Zolensky for their reviews. F. J. M. R. was supported by grant NNG05GM84G from the NASA Headquarters Stardust Participating Scientist program (Stardust) for HRTEM analyses conducted in the Electron Microbeam Analyses Facility housed in the Department of Earth and Planetary Sciences (UNM). T. N. was supported by a Grant-in-aid of the Japan Ministry of Education, Culture, Sports, Science and Technology (nos. 16340174 and 17654112). H. L. was supported by the Centre National des Études Spatiales. We thank Prof. K. Tomeoka, who allowed us to cite his data on similar inclusions in track #44.

Editorial Handling—Dr. Donald Brownlee

REFERENCES

Anand M., Taylor L. A., Nazarov M. A., Shu J., Mao H.-K., and Hemley R. J. 2004. Space weathering on airless planetary bodies: Clues from the lunar mineral hapkeite. *Proceedings of the National Academy of Sciences* 101:6847–6851.

Anderson W. and Ahrens T. J. 1994. Physics of interplanetary dust capture via impact into organic foam. *Journal of Geophysical Research* E99:2063–2071.

Badjukov D. D. and Petrova T. L. 1992. Shock-induced interaction between metal iron and silicates (abstract). 22nd Lunar and Planetary Science Conference. pp. 41–42.

Barrett R. A., Zolensky M. E., Hörz F., Lindstrom D. J., and Gibson E. K. 1992. Suitability of silica aerogel as a capture medium for interplanetary dust. Proceedings, 22nd Lunar and Planetary Science Conference. pp. 203–212.

Bradley J. P. 1994. Chemically anomalous, pre-accretionally irradiated grains in interplanetary dust from comets. *Science* 265: 925–929.

Burchell M. J., Graham G., and Kearsley A. 2006. Cosmic dust collection in aerogel. *Annual Review of Earth and Planetary Science* 34:385–418.

Essene E. J. and Fisher D. C. 1986. Lightning strike fusion: Extreme reduction and metal-silicate liquid immiscibility. *Science* 234: 189–193.

Hansen M. 1958. *Constitution of binary alloys*. New York: McGraw-Hill Book Company. pp. 704–708.

Jones B. E., Jones K. S., Rambo K. J., Rakov V. A., Jerald J., and Uman M. A. 2005. Oxide reduction during triggered-lightning fulgurite formation. *Journal of Atmospheric and Solar-Terrestrial Physics* 67:423–428.

Khalaff K. and Schubert K. 1974. Kristallstruktur von Fe_2Si(h). *Journal of the Less-Common Metals* 35:341–345.

Keil K., Berkley J. L., and Fuchs L. H 1982. Suessite, Fe_3Si: A new mineral in the North Haig ureilite. *American Mineralogist* 67: 126–131.

Kullerud G., Yund R. A., and Moh G. H. 1969. Phase relations in the Cu-Fe-S, Cu-Ni-S, and Fe-Ni-S systems. In *Magmatic ore deposits*, edited by Wilson H. D. B. Economic Geology Monograph 4. pp. 323–343.

Lattimer J. M. and Grossman L. 1978. Chemical condensation sequences in supernova ejecta. *Moon and Planets* 19:169–184.

Leroux H., Rietmeijer F. J. M., Velbel M. A., Brearley A. J., Jacob D., Langenhorst F., Bridges J. C., Zega T. J., Stroud R. M., Cordier P., Harvey R. P., Lee M., Gounelle M., and Zolensky M. E. 2008. A TEM study of thermally modified comet 81P/Wild 2 dust particles by interactions with the aerogel matrix during the Stardust capture process. *Meteoritics & Planetary Science* 43. This issue.

Nakamura T., Tsuchiyama A., Akaki T., Uesugi K., Nakano T., and Noguchi T. 2008. Bulk mineralogy and three-dimensional tomography of individual Stardust particles deduced from synchrotron X-ray diffraction and micro CT analysis. *Meteoritics & Planetary Science* 43. This issue.

Nuth J. A. and Donn B. 1982. Experimental studies of the vapor phase nucleation of refractory compounds. 1. The condensation of SiO. *Journal of Chemical Physics* 77:2639–1646.

Nuth J. A. III, Hallenbeck S. L., and Rietmeijer F. J. M. 1999. Interstellar and interplanetary grains—Recent developments and new opportunities for experimental chemistry. In *Laboratory astrophysics and space research,* edited by Ehrenfreund P., Krafft K., Kochan H., and Pirronello V. Dordrecht: Kluwer. pp. 43–182.

Nuth J. A. III, Hallenbeck S. L., and Rietmeijer F. J. M. 2000. Laboratory studies of silicate smokes: Analog studies of circumstellar materials. *Journal of Geophysical Research* 105: 10,387–10,396.

Nuth J. A. III, Rietmeijer F. J. M., and Hill H. G. M. 2002. Condensation processes in astrophysical environments: The composition and structure of cometary grains. *Meteoritics & Planetary Science* 37:1579–1590.

Okudaira K., Noguchi T., Nakamura T., Sugita S., Sekine Y., and Yano H. 2004. Evaluation of mineralogical alteration of micrometeoroid analog materials captured in aerogel. *Advances in Space Research* 34:2299–2304.

Okudaira K., Yano H., Noguchi T., Nakamura T., Burchell M. J., and Cole M. J. 2005. Are they really intact?—Evaluation of captured micrometeoroid analogs by aerogel at the fly-by speed of

Stardust (abstract #1832). 36th Lunar and Planetary Science Conference. CD-ROM.

Ramírez-Cardona M., Flores-Castro K., Cortés-García P. P., and Ortiz-Hernández L. E. 2006. Mineralogical study of binary iron silicides (Fe-Si system) in a fulgurite from Hidalgo, Mexico. *Boletín de Mineralogía* 17:69–76.

Rietmeijer F. J. M. 1998. Interplanetary dust particles. In *Planetary materials*, edited by Papike J. J. Reviews in Mineralogy, vol. 36. Chantilly, Virginia: Mineralogical Society of America. pp. 2-1–2-95.

Rietmeijer F. J. M. 2002. The earliest chemical dust evolution in the solar nebula. *Chemie der Erde* 62:1–45.

Rietmeijer F. J. M. and Karner J. M. 1999. Metastable eutectic gas to solid condensation in the Al_2O_3-SiO_2 system. *Journal of Chemical Physics* 110:4554–4558.

Rietmeijer F. J. M., Karner J. M., Nuth J. A. III, and Wasilewski P. J. 1999b. Nanoscale phase equilibrium in a triggered lightning strike experiment. *European Journal of Mineralogy* 11:181–186.

Rietmeijer F. J. M., Nuth J. A. III, and Karner J. M. 1999a. Metastable eutectic gas to solid condensation in the FeO-Fe_2O_3-SiO_2 system. *Physical Chemistry Chemical Physics* 1:1511–1516.

Rietmeijer F. J. M., Nuth J. A. III, Jablonska M., and Karner J. M. 2000. Metastable eutectic equilibrium in natural environments: Recent developments and research opportunities. *Trends in Geochemistry* 1:29–51.

Rietmeijer F. J. M., Nuth J. A. III, Karner J. M., and Hallenbeck S. L. 2002. Gas to solid condensation in a Mg-SiO-H_2-O_2 vapor: Metastable eutectics in the MgO-SiO_2 phase diagram. *Physical Chemistry Chemical Physics* 4:546–551.

Rowan L. R. and Ahrens T. J. 1994. Observations of impact-induced molten metal-silicate partitioning. *Earth and Planetary Science Letters* 122:71–88.

Sandford S. A., Aléon J., Alexander C. M. O'D., Araki T., Bajt S., Baratta G. A., Borg J., Brucato J. R., Burchell M. J., Busemann H., Butterworth A., Clemett S. J., Cody G., Colangeli L., Cooper C., D'Hendecourt L., Djouadi Z., Dworkin J. P., Ferrini G., Fleckenstein H., Flynn G. J., Franchi I. A., Fries M., Gilles M. K., Glavin D. P., Gounelle M., Grossemy F., Jacobsen C., Keller L. P., Kilcoyne A. L., Leitner J., Matrajt G., Meibom A., Mennella V., Mostefaoui S., Nittler L. R., Palumbo M. E., Robert F., Rotundi A., Snead C. J., Spencer M. K., Steele A., Stephan T., Tyliszczak T., Westphal A. J., Wirick S., Wopenka B., Yabuta H., Zare R. N., and Zolensky M. 2006. Organics captured from comet 81P/Wild 2 by the Stardust spacecraft. *Science* 314:1720–1724.

Sheffer A. A., Melosh H. J., Jarnot B. M., and Lauretta D. S. 2003. Reduction of silicates at high temperature: Fulgurites and thermodynamic modeling (abstract #1467). 34th Lunar and Planetary Science conference. CD-ROM.

Uesugi K., Takeuchi A., and Suzuki Y. 2006. Development of microtomography system with Fresnel zone plate optics at SPring-8. In Developments in X-ray tomography V, edited by Bonse U. Bellingham, Washington: SPIE. 1 vol.

Wasserman A. A. and Melosh H. J. 2001. Chemical reduction of impact processed materials (abstract #2037). 32nd Lunar and Planetary Science Conference. CD-ROM.

Wasserman A. A., Melosh H. J., and Lauretta D. S. 2002. Fulgurites: A look at transient high-temperature processes in silicates (abstract #1308). 33rd Lunar and Planetary Science Conference. CD-ROM.

Wever F. 1928. Ueber den Einfluß der Elementen aud den Polymorphismus des Eisens. *Archiv für des Eisenhüttenwesen* 11:1929–2, 739–748.

Yu Z. 1984. Two new minerals gupeiite and xifengite in cosmic dusts from Yanshan. *Acta Petrologica Mineralogica Analytica* 3:231–238.

Zolensky M., Zega T. J., Yano H., Wirick S., Westphal A. J., Weisberg M. K., Weber I., Warren J. L., Velbel M. A., Tsuchiyama A., Tsou P., Toppani A., Tomioka N., Tomeoka K., Teslich N., Taheri M., Susini J., Stroud R., Stephan T., Stadermann F. J., Snead C. J., Simon S. B., Simionovici A., See T. H., Robert F., Rietmeijer F. J. M., Rao W., Perronnet M. C., Papanastassiou D. A., Okudaira K., Ohsumi K., Ohnishi I., Nakamura-Messenger K., Nakamura T., Mostefaoui S., Mikouchi T., Meibom A., Matrajt G., Marcus M. A., Leroux H., Lemelle L., Le L., Lanzirotti A., Langenhorst F., Krot A. N., Keller L. P., Kearsley A. T., Joswiak D., Jacob D., Ishii H., Harvey R., Hagiya K., Grossman L., Grossman J. N., Graham G. A., Gounelle M., Gillet Ph., Genge M. J., Flynn G., Ferroir T., Fallon S., Ebel D. S., Dai Z. R., Cordier P., Clark B., Chi M., Butterworth A. L., Brownlee D. E., Bridges J. C., Brennan S., Brearley A., Bradley J. P., Bleuet P., Bland P. A., and Bastien R. 2006. Mineralogy and petrology of comet 81P/Wild 2 nucleus samples. *Science* 314:1735–1739.